Supporting Information for

Orientation-Independent-DIC imaging reveals that a transient rise in depletion attraction contributes to mitotic chromosome condensation

Shiori Iida, Satoru Ide, Sachiko Tamura, Masaki Sasai, Tomomi Tani, Tatsuhiko Goto, Michael Shribak*, Kazuhiro Maeshima*

*Correspondence: Kazuhiro Maeshima or Michael Shribak
Email: kmaeshim@nig.ac.jp or mshribak@mbl.edu

This PDF file includes:

Materials and Methods
Figures S1 to S11
Tables S1 to S2
Legends for Movie S1
SI References

Other supporting materials for this manuscript include the following:

Movie S1

Materials and Methods

Cell lines and establishment of stable cell lines.

HCT116 cells (CCL-247; ATCC) were cultured at 37 °C and 5% CO_2 in McCoy's 5A medium (SH30200.01; HyClone) supplemented with 10% fetal bovine serum (FBS; FB-1061/ 500; Biosera). Indian Muntjac DM cells were a generous gift from Dr. H. Kimura and Dr. P. Cook (Tokyo Tech and Oxford University, respectively) (1). The cells were cultured at 37 °C and 5% CO_2 in Dulbecco's Modified Eagle's medium (DMEM; D5796- 500ML; Sigma-Aldrich) supplemented with 20% FBS.

The transposon system was used to stably express H2B-Halo in the HCT116 cell line. The constructed plasmid pPB-CAG-IB-H2B-HaloTag (2) was cotransfected with pCMV-hyPBase (provided by Sanger Institute with a materials transfer agreement) into HCT116 cells with the Effectene transfection reagent kit. Transfected cells were then selected with 10 μg/mL blasticidin S. HCT116 cells expressing SMC2-mAID-mClover and Tet-OsTIR1 were used as parental cells (3, 4).

pPB-CAG-mCherry-NPM1 plasmid was constructed based on pPB-CAG-IB (provided from Sanger Institute with a materials transfer agreement). Full length NPM1 fused to EGFP at the N-terminus was cloned into pEF1-FRT plasmid (5). From pEF1-EGFP-NPM1-FRT, the coding region of NPM1 was amplified using the following primer pairs: 5'-GACGAGCTGTACAAGGGTGGAGGTGGATCTGGTGGAG-3' and 5'-GGGGCGGAATTCGTTTTAAAGAGACTTCCTCCACTGCCAG-3'. The mCherry fragment was amplified from pmCherry_a_tubulin_IRES_puro2 (#21043, Addgene) using the following primers: 5'- GAATTGATCTCTCGAGATGGTGAGCAAGGGCGAGGAG-3' and 5'-CTTGTACAGCTCGTCCATGCC-3'. The amplified fragments were joined together using standard overlapping PCR and inserted into pPB-CAG-IB-H2B-HaloTag digested with XhoI and HpaI using In-Fusion (639650; Takara). To stably express mCherry-NPM1 in HCT116 cell line, the transposon system was used. The constructed plasmid pPB-CAG-mCherry-NPM1 was cotransfected with pCMV-hyPBase into HCT116 cells expressing mAID-mClover-RPA194 (6) with the Neon Electroporation System (MPK5000; Thermo Fisher Scientific). For the electroporation, cells were resuspended in Neon Resuspension Buffer R (10 μL, Neon kit, Invitrogen) to a final concentration of 2.5×10^7 cells/mL and mixed with 500 ng of pPB-CAG-mCherry-NPM1 and pCMV-hyPBase, respectively. The mixture was pulsed once with a voltage of 1400 and a width of 20. Transfected cells were then selected with 10 μg/mL blasticidin S (029–18701; Wako).

Description of OI-DIC/confocal setup.

A simplified optical schematic of the confocal laser scanning microscope Olympus FV3000 (Evident, Tokyo, Japan) with the OI-DIC module is shown in Fig. 1B. The FV3000 consists of an inverted microscope Olympus IX83, a confocal scan unit, and a laser combiner. The microscope IX83 was equipped with a 100-W halogen lamp U-LH100L-3, a bandpass filter 546/10 nm (Chroma, Bellows Falls, VT, USA), a condenser IX2-DICD with front lens U-TLD 0.9NA, a water immersion objective lens UPlanSApo 60X/1.2NA W, and an 8-positions mirror turret FV30-RFACA. The condenser, objective lens, and specimen under investigation were placed in a Thermo Box IX83TB (Tokai Hit, Shizuoka, Japan). The turret contains an LSM mirror and analyzer cube IX3-FDICT. Regular Olympus DIC sliders were replaced by custom beam-shearing DIC assemblies. The first assembly consists of a pair of DIC prisms U-ODIC100HR, a liquid crystal polarization rotator, and a liquid crystal variable retarder (ARCoptix, Neuchatel, Switzerland). The second assembly consists of a pair of DIC prisms U-DICTHR and a liquid crystal polarization rotator. The assemblies can quickly switch the shear direction by 90º and change the bias without any mechanical movement. A set of 4 or 6 DIC images was captured by a digital camera Infinity 3-1M (Lumenera, Ottawa, Canada). More details about OI-DIC image acquisition and processing were described previously (7, 8). The laser combiner has four laser diodes with wavelengths of 405 nm, 488 nm, 562 nm, and 640 nm. Their beam intensities were controlled by an acousto-optic tunable filter and then delivered by a single-mode optical fiber to a confocal scan unit. Excitation dichroic mirror reflects the laser light to a pair of Galvano scanning mirrors and CLSM mirror. The emission light is transmitted by the dichroic mirror to an adjustable confocal pinhole and 2-channel multi-alkali PMT spectral detector unit FV31-SD. The spectral detector employs efficient Volume Phase Holographic transmission grating and adjustable slit with 1–100 nm bandwidth from a 400–800 nm detection region.

Mathematical model of OI-DIC microscopy

For the convenience of the reader, we briefly explain the mathematical principles of the OI-DIC technique and one of image processing algorithms. The OI-DIC mathematical model, along with several processing algorithms, were reported in detail elsewhere (8-11).

The intensity distribution in the DIC image $I(x,y)$ can be described by using a model of interference of two overlapping identical coherent images with an optical path difference $OPD(x,y)$, slightly offset from each other:

$$I(x,y) = \tilde{I}\sin^2\left\{\frac{\pi}{\lambda}[\Gamma + \mathbf{d}\cdot\mathbf{G}(x,y)]\right\} + I_c\,(x,y),$$

where $\tilde{I}$ is the initial beam intensity, λ is the wavelength, Γ is the bias, $\mathbf{d}$ is the shear vector, $\mathbf{G}(x,y)$ is the optical path difference gradient vector, and $I_c(x,y)$ corresponds to an offset of the intensity signal, which is caused by the stray light.

The optical path difference gradient vector **G**(*x,y*) is the following:

$$\mathbf{G}(x,y)=\left(\frac{d(OPD(x,y))}{dx},\frac{d(OPD(x,y))}{dy}\right)=\left(\gamma(x,y)\cos\theta(x,y),\gamma(x,y)\sin\theta(x,y)\right),$$

where $\gamma(x,y)$ and $\theta(x,y)$ are the optical path difference gradient magnitude and azimuth, respectively.

In order to map the optical path difference gradient vector **G**(*x,y*), the OI-DIC microscope varies shear vector $\boldsymbol{d}$ and bias Γ. We capture two sets of raw DIC images at shear directions 0º (X-shear) and 90º (Y-shear) with negative, zero, and positive biases: $-\Gamma_0$, 0, and $+\Gamma_0$. Typically, we use biases of ±0.15λ and 0.

The following group of equations represents these six DIC images:

$$I_{i,j}(x,y)=\tilde{I}\cdot\sin^2\left\{\frac{\pi}{\lambda}[j\cdot\Gamma_0-d\cdot\gamma(x,y)\sin(\theta(x,y)-i\cdot 90°)]\right\}+I_{min}(x,y),$$

where *i*=1 and *i*=2 represent X- and Y-shears, respectively, *j* = -1, 0, 1 corresponds to three settings of the bias, *d* is the shear amount (magnitude of shear vector), and $I_{min}(x,y)$ corresponds to an offset of the intensity signal, which is caused by the stray light.

Initially two terms are computed (*i* = 1, 2):

$$A_i(x,y)=\frac{I_{i,1}(x,y)-I_{i,-1}(x,y)}{I_{i,1}(x,y)+I_{i,-1}(x,y)-2I_{i,0}(x,y)}\tan\left(\frac{\pi\Gamma_0}{\lambda}\right).$$

Using the obtained terms, we can calculate the quantitative two-dimensional distributions of the gradient magnitude and azimuth of an optical path difference in the specimen as:

$$\gamma(x,y)=\frac{\lambda}{2\pi d}\sqrt{\sum_{i=1}^{2}\arctan^2[A_i(x,y)]},$$

$$\theta(x,y)=\arctan\left[\frac{\arctan(A_2(x,y))}{\arctan(A_1(x,y))}\right].$$

The gradient magnitude represents an increment of the optical path difference, which is in nanometers, along a lateral coordinate, which is also in nanometers. Thus, the gradient magnitude is unitless.

The obtained two-dimensional distribution of the optical path difference gradient vector **G**(*x,y*) is used for computing the optical path difference map *OPD(x,y)*. For this purpose, the gradient vector **G**(*x,y*) can be presented as a complex number:

$$\mathbf{G}(x,y) = \frac{\partial(OPD(x,y))}{\partial x} + i\frac{\partial\phi(OPD(x,y))}{\partial y} = \gamma(x,y)e^{i\theta(x,y)}, \quad (1)$$

where real and imaginary parts are X- and Y- components of the gradient vector, respectively.

At first, we apply the 2-dimensional Fourier transform to the left and middle parts of the equation above. The resultant integral equation can be solved by partial integration. After using the inverse 2-dimensional Fourier transform we receive the following formula for computation of the optical path difference *OPD(x,y)*:

$$OPD(x,y) = F^{-1}\left[\frac{F\left[\mathbf{G}(x,y)\right]}{i(\omega_x + i\omega_y)}\right],$$

where ω_x and ω_y are spatial angular frequencies.

Considering the right part of equation (1), we finally obtain the formula for computing the OPD:

$$OPD(x,y) = F^{-1}\left[\frac{F\left[\gamma(x,y)e^{i\theta(x,y)}\right]}{i(\omega_x + i\omega_y)}\right].$$

Then a computed two-dimensional distribution of the optical path difference is transformed into quantitative 8-bit grayscale image (map), where the image brightness is linearly proportional to value of the OPD and the maximum gray level of 255 corresponds to the chosen OPD ceiling.

OI-DIC imaging of glass rods.

A small number of glass rods 4 μm in diameter were suspended in two types of mineral oil with refractive indices of 1.54 and 1.58. Approximately 2 μL of the suspended solution was sandwiched between a glass slide and a coverslip and then sealed with nail polish. The glass rods in the mineral oil were analyzed by OI-DIC microscopy using the same procedure as the live cell imaging. A plot of the intensity profile across a glass rod was created by ImageJ (line width: 10 pixels) to validate density imaging by OI-DIC microscopy. The theoretical OPD curve was calculated based on the thickness and the RI of a glass rod, assuming that the cross-section of the glass rod is a circle with a diameter of 4 μm.

Measurement of the Refractive Index (RI) of standard solutions.

To obtain calibration curves of the RIs of proteins and nucleic acids (Fig. 1D (iii)), bovine serum albumin (BSA; Sigma; A9647-100G) and salmon sperm DNA (WAKO; 043-31381) were dissolved in water at concentrations of 0–300 and 0–30 mg/mL, respectively. The RIs of the prepared standard solutions were measured with a refractometer, Abbé-3L (Bausch & Lomb). The

measured RIs and solution densities were plotted and fitted with linear functions to obtain calibration curves ($RI = 1.333 + 1.65 \times 10^{-4} \times C$, where C is the density). RI of the medium was also measured by the same refractometer. The RI of McCoy's 5A/10% FBS was 1.3362 and the RI of DMEM/20% FBS was 1.3379.

Cell preparation.

Cells were seeded on 24 mm × 24 mm square glass coverslips coated with 2.5 μg/mL fibronectin (354008; Corning) diluted in PBS for 1 h at 37 °C and cultured for 1–2 days. In HCT116 cells, cytoplasm and histone H2B-Halo were labeled with 3 μg/mL Calcein-AM and 5 nM TMR, respectively, for 30 min at 37 °C in 5% CO_2, then washed with 1× HBSS (H1387; Sigma-Aldrich) three times. In DM cells, DNA was stained with 1.8 μg/mL Hoechst33342 (H342; Dojindo) instead of TMR. Cells were then incubated in the following phenol red-free media. HCT116 cells were observed in McCoy's 5A (1-18F23-1; BioConcept) with 10% FBS, and DM cells were observed in DMEM (21063-029; Thermo Fisher Scientific) with 20% FBS. The cells were mounted on a glass slide with a silicone spacer having a thickness of 0.5 mm. We observed the mounted cells by OI-DIC and fluorescence imaging. Cells were not synchronized.

Live-cell OI-DIC microscopy imaging.

Before the experiment, the Thermo Box was set at 37 °C. The specimen was placed on the microscope stage, and the microscope was switched to the DIC mode. The analyzer was in the beam path, and the LSM mirror was out. The camera showed a live DIC image. The objective lens was focused on the middle plane of the cell under investigation. Using the custom software, which controlled the beam-shearing assemblies, we captured a set of DIC images with X- and Y-shear directions. We took 3 images in each direction, with zero and ±0.15λ biases. The total acquisition time of six images was about 1 s. The corresponding background image without cells or structures was also taken prior to each image acquisition to create the OPD map. The captured images were processed according to the previously reported algorithm (8), and the OPD map was generated (7) (Fig. S1B). In the next step, the microscope was switched to the confocal mode. The analyzer was out of the beam path, and the LSM mirror was in. Then, optical sectioning images were recorded in the confocal mode with a 0.5 μm step size, using 405, 488, and 561 nm lasers for Hoechst33342, Calcein-AM, and TMR, respectively.

Density estimation of cellular contents.

This OI-DIC version allowed the OI-DIC image and confocal images to be obtained in the same field of view. Therefore, it was possible to estimate both the OPD and thickness at a particular point and obtain an accurate molecular density at that point. The OPD was proportional to the thickness of a sample and the difference in RI between the sample and the surrounding solution,

as shown in Fig. 1D(ii). Therefore, we calculated the RI of samples based on the RI of the surrounding solution and sample thickness (Fig. 1D(i), (ii)).

First, we cropped the OPD map to manually match the field of the confocal image captured by CLSM using intracellular structures (e.g., nuclei) as indicators. Second, to calculate the Optical Path Difference (OPD) between the medium and samples, we obtained the Optical Path Length (OPL) of medium, OPL_{med}, and OPL of sample, OPL_s. The pixel intensity of OPD map reflects OPL at that location. To obtain OPL_{med}, we set 5 ROIs [circles with a diameter of ~0.6 μm] outside of cells and calculated the mean intensity inside the ROIs. For OPL_s, we placed the ROIs at the several selected points within the sample (Fig. S2). When calculating cytoplasmic OPL (OPL_{cy}), the ROIs were set to avoid apparent structures in the Riesz image and chromosomes in the entire z-stacks (Fig. S2). We calculated OPD for each point as the difference between OPL_{cy}, for that point and OPL_{med}. The thickness of the sample (t) at the same points where we obtained the OPD was determined using the corresponding confocal image. The intensity threshold for calculating thickness was set at the specific value based on the difference between the maximum and minimum intensity of the z-axis profile at the ROI (also see Figs. S3C, S4A, and S4C). To calculate the thicknesses of prophase, telophase, and early G1 nuclei, a Gaussian blur filter (σ = 20) was applied to the chromatin channel before setting the threshold.

Then, we calculated the dry mass density ("density" for short) for each point of the cytoplasm using the following formula:

$$RI_S = RI_{med} + OPD/t,$$

where RI_{med} is the refractive index of the surrounding medium.
RI_{med} was measured as 1.3362 (McCoy's 5A/10% FBS) and 1.3379 (DMEM/20% FBS). We determined the density of the sample from its RI using our calibration curves (Fig. 1D(iii); $RI = 1.333 + 1.65 \times 10^{-4} \times C$, where C is the density). To plot cytoplasm density of a cell, we calculated the mean of the density values measured within that cell. Also see "Measurement of Refractive Index (RI) of standard solutions"; Figs. 1D, 2B, and S3A.

To identify the density of the nucleus, we calculated the OPD of the nucleus and cytoplasm, OPD_{nu-cy}, for all the combination pairs of the selected points at cytoplasm and nucleus. We then obtained the average OPD_{nu-cy} at each specific point, according to the procedure in Fig. S3B (7). We multiplied cytoplasm OPL that does not cross the nucleus (OPL_{cy}) by the ratio (t_2/t_1) of the cytoplasm thickness that crosses the nucleus (t_2) to the cytoplasm thickness that does not cross nucleus (t_1) because the thicknesses of these two polarized beams passed through the sample should be the same. Subsequently, we calculated the density at each point of nucleus using the

measured OPD_{nu-cy}, RI_{cy}, and the thickness of nucleus at that point. Finally, we derived the mean of the density values measured within the cell as the nucleoplasm density of that cell. The process for measuring the density of chromosomes followed the same methodology as for nucleoplasm (see Fig. S4B-C). All measurements were done using FIJI software. Graphs were plotted using R.

Classification of cell cycle stages.

Mitotic cells were selected for density imaging from an asynchronous cell population. The classification of cells was based on the following criteria:

- Interphase: Flat, adhered cells with visible nuclear envelope and without visible chromosomes.
- Prophase: Adhered cells with visible nuclear envelope, initiating chromosome condensation.
- Prometaphase: Round-shaped cells with chromosomes not aligned around the center.
- Metaphase: Round-shaped cells with chromosomes aligned around the center.
- Anaphase: Cells where sister chromosomes have started to separate.
- Telophase: Cells with visible nuclear envelope, where cytokinesis has started.
- Early G1: Cells with visible nuclear envelope, where cytokinesis is complete.

Also, refer to Fig. S2 for visual representation. In DM cells, anaphase and telophase cells moved during observation, preventing accurate density calculation.

Hypertonic and hypotonic treatment.

For hypertonic treatment, cells were incubated in a medium supplemented with 0.9 mL medium and 0.1 mL 10× PBS just before observation. Cells were observed by OI-DIC within 1 h. For hypotonic treatment, cells were incubated in a mixture of 1 mL medium and 1 mL MilliQ water just before observation. Cells were observed by OI-DIC within 1 h. The RIs of the media: 1.3379 (McCoy's 5A/10% FBS, hypertonic), 1.3349 (McCoy's 5A/10% FBS, hypotonic) and 1.3403 (DMEM/20% FBS, hypertonic), 1.3357 (DMEM/20% FBS, hypotonic).

Chromatin/DNA compaction analysis.

To quantify DNA density, we used the obtained confocal images. In a central z-section of a mitotic cell (determined by visual inspection based on the largest area of cytoplasm), the DNA channel was denoised using a Gaussian blur filter ($\sigma = 2$) and threshold set using the Otsu dark method in FIJI. The resulting binary mask was converted into a selection, and the DNA mean fluorescence within this ROI was measured. All data points were normalized to the mean of unperturbed control cells. For hypotonic treatment, only images taken within 10 min after treatment were used.

Chromatin preparation, condensation/droplet formation assay, and droplet imaging. Fresh chicken blood was obtained from the wing vein of Tosa-jidori. Preparation of chicken native chromatin was as described previously (12). Briefly, 2 mL of fresh chicken blood was lyzed with 20 mL of MLB (60 mM KCl, 15 mM NaCl, 15 mM HEPES-KOH (pH 7.3), 2 mM $MgCl_2$, 0.1% NP-40, and 1 mM phenyl-methylsulfonyl fluoride [PMSF]) for 10 min on ice. After centrifugation at 1200 × *g* at 4 °C for 5 min, the supernatant was removed and resuspended in 20 mL of MLB. This step was repeated four times before the samples were ready for chromatin purification. Chromatin purification was carried out as described by (13), with some modifications. The nuclei (equivalent to ~2 mg of DNA) in nuclei isolation buffer (10 mM Tris-HCl, pH 7.5, 1.5 mM $MgCl_2$, 1.0 mM $CaCl_2$, 0.25 M sucrose, 0.1 mM PMSF) were digested with 50 U of micrococcal nuclease (Worthington, Lakewood, NJ) at 30 °C for 2 min. The reaction was stopped by adding ethylene glycol tetraacetic acid (EGTA) to a final concentration of 2 mM. After being washed with nuclei isolation buffer, the nuclei were lyzed with lysis buffer (10 mM Tris-HCl (pH 8.0), 5 mM EDTA, 0.1 mM PMSF) on ice for 5 min. The lysate was dialyzed against dialysis buffer (10 mM HEPES-NaOH (pH 7.5), 0.1 mM EDTA, 0.1 mM PMSF) at 4 °C overnight using Slide-A-Lyzer (66380 Thermo Scientific). The dialyzed lysate was centrifuged at 20400 × *g* at 4 °C for 10 min. The supernatant was recovered and used as the purified chromatin fraction. The purity and integrity of the chromatin protein components were verified by 14% SDS–PAGE (Fig. S8A). To examine the average DNA length of the purified chromatin, DNA was isolated from the chromatin fraction and electrophoresed in a 0.7% agarose gel (Fig. S8B).

Samples of chicken chromatin (4 µg) were incubated with 10 mM HEPES-NaOH (pH 7.5), 0.8 mM $MgCl_2$, 100 mM KCl, and indicated concentration of crowder in 200 µL of a reaction mixture at room temperature for 30 min. The mixture (10 µL) was mounted on a glass slide with 2 µL of DAPI solution (82 µg/mL). The coverslips were sealed with nail polish. The crowders used were polyethylene glycol (PEG; P5413, Sigma-Aldrich), Dextran (180~210 kDa, 041-22612, Fujifilm), and bovine serum albumin (BSA; BAC65, Equitech-Bio, Inc), and first dissolved in a buffer containing 10 mM HEPES-NaOH (pH 7.5) and 0.1 mM EDTA as 30% (w/v) solution. ImageJ was used to measure the droplet diameter by converting droplet images to binary images with a threshold of 80-255. Droplet diameters were then measured using "Analyze Particles".

For the chromatin assays at 40 mg/mL PEG, 200 mg/mL BSA, or 100 mg/mL Dextran (Panel 4 in Figs. 6A, 6C, and S8C), the chromatin droplets were first formed at 20 mg/mL PEG, 100 mg/mL BSA, or 50 mg/mL Dextran, and then additional crowder was added.

For the droplet dilution assays (Figs. 6E, 6F, and S8D), chromatin droplets were first formed at 20 mg/mL PEG, 100 mg/mL BSA, or 50 mg/mL Dextran. Then, 9 volumes of a dilution buffer

containing 10 mM HEPES-NaOH (pH 7.5), 0.8 mM $MgCl_2$, 100 mM KCl with or without crowder were added, incubated for 3 h and mounted with DAPI as described above.

For the chromatin droplet imaging, optical sectioning images were recorded with a 200 nm step size using a DeltaVision microscope (Applied Precision) and deconvolved to remove out-of-focus information. Projected images from five sections were shown as described previously (14).

Density imaging and estimation of native chromatin droplets

The chromatin droplets were prepared for density imaging (Fig. S9), as described in the section "Chromatin preparation, condensation/droplet formation assay, and droplet imaging". The chromatin droplet solution was mounted with 18 mm × 18 mm square glass coverslips with DAPI. Imaging of the droplets was performed as outlined in the "Live-cell OI-DIC microscopy imaging" section, but at room temperature with a 0.25 μm step size, using an oil immersion 60X objective lens (Olympus PLAPON 60XO NA: 1.42).

To calculate the density inside droplets, solutions with various concentrations of PEG or BSA, containing 100 mM K^+ and 0.8 mM Mg^{2+}, were measured with a refractometer, Abbé-3L. The measured RIs and solution densities were plotted and fitted with linear functions to obtain calibration curves. The resulting calibration formula was $RI = 1.333 + 1.39 \times 10^{-4} \times C$, where C is the density.

Density inside droplets was estimated using the same procedure described in the section "Density estimation of cellular contents" (also see Fig. 1D). Briefly, on the OPD map, we set 6 ROIs outside of the droplets to obtain $OPL_{solution}$ and 4-8 ROIs inside the droplets to obtain $OPL_{droplet}$. Their difference, $OPD_{droplet-solution}$, was then calculated. The intensity threshold for determining droplet thickness (t) was set at 40% of the difference between the maximum and minimum intensity of the z-axis profile at the ROI. Then, we calculated the density for each point in the droplet using the formula $RI_{droplet} = RI_{solution} + OPD/t$. The $RI_{solution}$ values measured by the refractometer were 1.3365 for 20 mg/mL PEG, 1.3388 for 40 mg/mL PEG, 1.3478 for 100 mg/mL BSA, and 1.3608 for 200 mg/mL BSA. Finally, we calculated the mean of the density values measured within the droplet as the density inside the droplet and plotted these values on the graphs.

Immunostaining of ribosomal P protein.

HCT116 cells expressing SMC2-mAID-mClover were grown on the poly-L-lysine–coated (P1524-500MG, Sigma-Aldrich) coverslips (C018001, Matsunami) for 2 days. All following processes were performed at room temperature. The cells were fixed with 1.85% formaldehyde (064-00406,

Wako) on coverslips for 15 min, permeabilized with 0.5% Triton X-100 (T-9284, Sigma-Aldrich) for 5 min. After washing twice with HMK (20 mM HEPES (pH 7.5) with 1 mM $MgCl_2$ and 100 mM KCl) for 5 min, the cells were incubated with 10% normal goat serum (NGS; 143-06561, Wako) in HMK for 30 min. The cells were incubated with mouse anti-ribosomal p protein primary antibody (a gift from Dr. T. Uchiumi at Niigata University)(15) diluted 1:10000 in 1% NGS in HMK for 1 h. After being washed four times with HMK, the cells were incubated with goat anti–mouse IgG Alexa Fluor 594 (A11032, Thermo Fisher Scientific) secondary antibody diluted 1:1000 in 1% NGS in HMK for 1 h, followed by washing four times with HMK. Cells were then stained with 0.5 μg/mL 4',6-diamidino-2- phenylindole (DAPI; 10236276001, Roche) for 5 min, followed by PPDI [20 mM HEPES (pH 7.4), 1 mM $MgCl_2$, 100 mM KCl, 78% glycerol, and 1 mg/mL paraphenylene diamine (695106-1G, Sigma-Aldrich)] mounting. Optical sectioning images were recorded with a 0.5 μm step size using FV3000 confocal microscope equipped with an oil immersion 60X objective lens (Olympus UPlanXApo 60X NA: 1.42).

Estimation of depletion attraction in the cell.

We may consider chromosomes as arrays of *N* chromatin domains, each with a radius of $D \approx 100$ nm, and the depletant molecules as particles, each with a radius of $d \approx 3$ nm. The depletion attraction gives rise to the entropy gain (16) by juxtaposing a pair of spheres of radius *D* as

$$S_{\mathrm{pair}} = \left(1 + \frac{3}{2}\frac{D}{d}\right) n k_{\mathrm{B}}. \qquad (2)$$

Here, k_{B} is the Boltzmann constant and n is the volume fraction of the depletant molecules. Considering the depletant molecules to be 30 kDa proteins, the chromosome milieu density of 140 mg/mL in interphase and 170 mg/mL in mitotic anaphase amounts to $n = 0.31$ and 0.37, respectively. Using these values in Eq. 2, we find S_{pair} = 15.7k_{B} and 18.7k_{B} in interphase and mitotic anaphase, respectively. Then, the depletion force gains entropy S_{gain} upon condensation of a chromosome chain as $S_{\mathrm{gain}}^{\mathrm{inter}} = 15.7\left(\frac{z}{2}\right) n k_{\mathrm{B}}$ in interphase and $S_{\mathrm{gain}}^{\mathrm{mitotic}} = 18.7\left(\frac{z}{2}\right) n k_{\mathrm{B}}$ in mitotic anaphase, where z is the number of domains contacting to each domain estimated as $z = 4\sim6$ in a collapsed rod of the chromosome.

Chromosome condensation should increase free energy of $F_{\mathrm{loss}} = F_{\mathrm{domain}} + S_{\mathrm{loss}}T$, with F_{domain} arising from repulsion between domains and $S_{\mathrm{loss}}T$ being entropy loss caused by the constrained chain fluctuation upon condensation. Here, $S_{\mathrm{loss}}\sim n k_{\mathrm{B}}$ by neglecting the factor of order of one. Free energy decrease upon condensation is $F_{\mathrm{gain}} = F_{\mathrm{cond}} + S_{\mathrm{gain}}T$ with the condensin-caused interactions, F_{cond}, and the free energy stabilization through the depletion effect, $S_{\mathrm{gain}}T$. Chromosomes condense when F_{gain} exceeds F_{loss}. An increase in $S_{\mathrm{gain}}T$ due to the increase in the milieu density, $\delta S_{\mathrm{gain}}T = \left(S_{\mathrm{gain}}^{\mathrm{mitotic}} - S_{\mathrm{gain}}^{\mathrm{inter}}\right)T = 3\left(\frac{z}{2}\right) n k_{\mathrm{B}}T \approx 6\sim9 n k_{\mathrm{B}}T$ $(6\sim9 k_{\mathrm{B}}T/\mathrm{domain})$, is of

the same order of or larger than $S_{\mathrm{loss}}T$, showing the essential contribution of the depletion attraction to chromosome compaction.

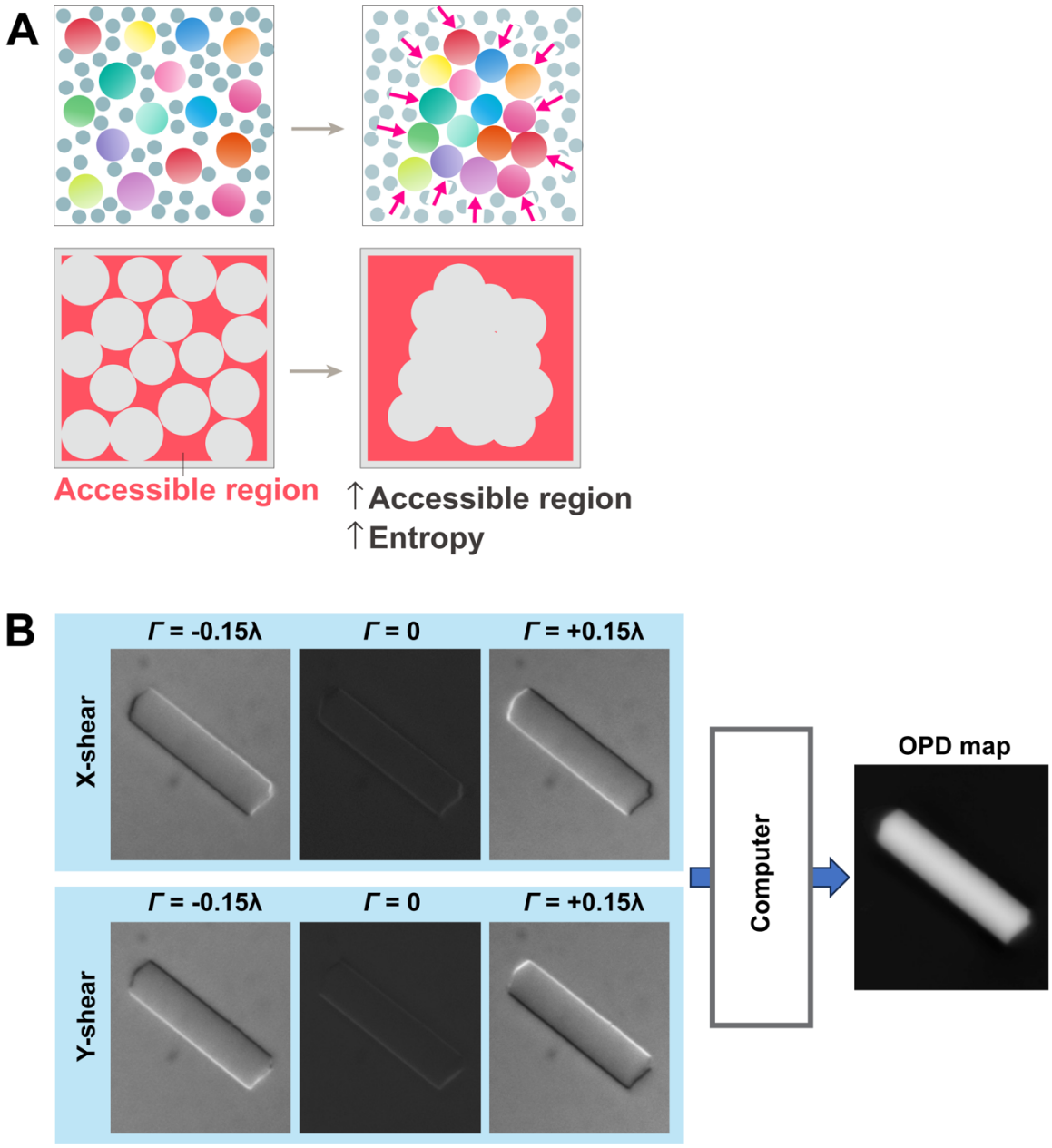

Figure S1.

Schematic for depletion attraction and the principle of OI-DIC imaging.

(A) Chromatin condensation by depletion attraction/macromolecular crowding effect. Chromatin domains/globules (colored spheres) are present in a square. The excluded volume is shown in gray. If chromatin domains associate with each other, the accessible region for soluble macromolecules (red) increases (excluded volume decreases). This state is then favored. **(B)** OI-DIC can rapidly switch the shear directions of DIC without mechanically rotating the specimen or the prisms (8). A set of raw DIC images with orthogonal shear directions and different biases is

captured within a second (Left). Specialized software computes a phase gradient vector map and then a quantitative phase image (Right).

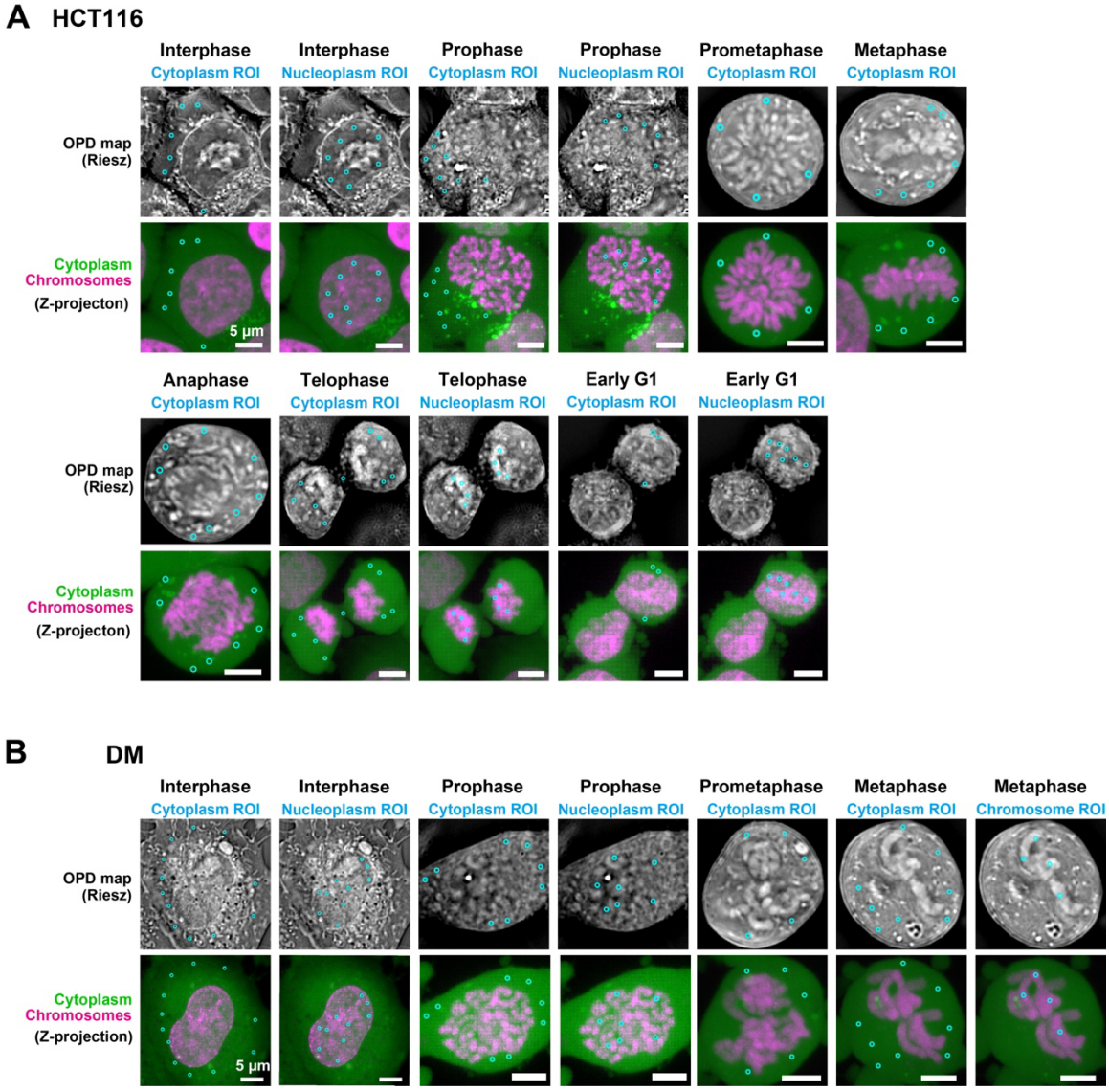

Figure S2.

ROIs set to estimate total density.

ROIs (small circles) used to estimate total density are shown in overlapping Riesz (Upper) and confocal (Lower) images in **(A)** HCT116 and **(B)** DM cells. Note that the ROIs avoid apparent structures in Riez images, presumably endoplasmic reticulum, Golgi apparatus, mitochondria, and nucleoli. Selection of ROIs avoids chromosomes in mitosis when measuring cytoplasm density and areas where multiple cells overlap.

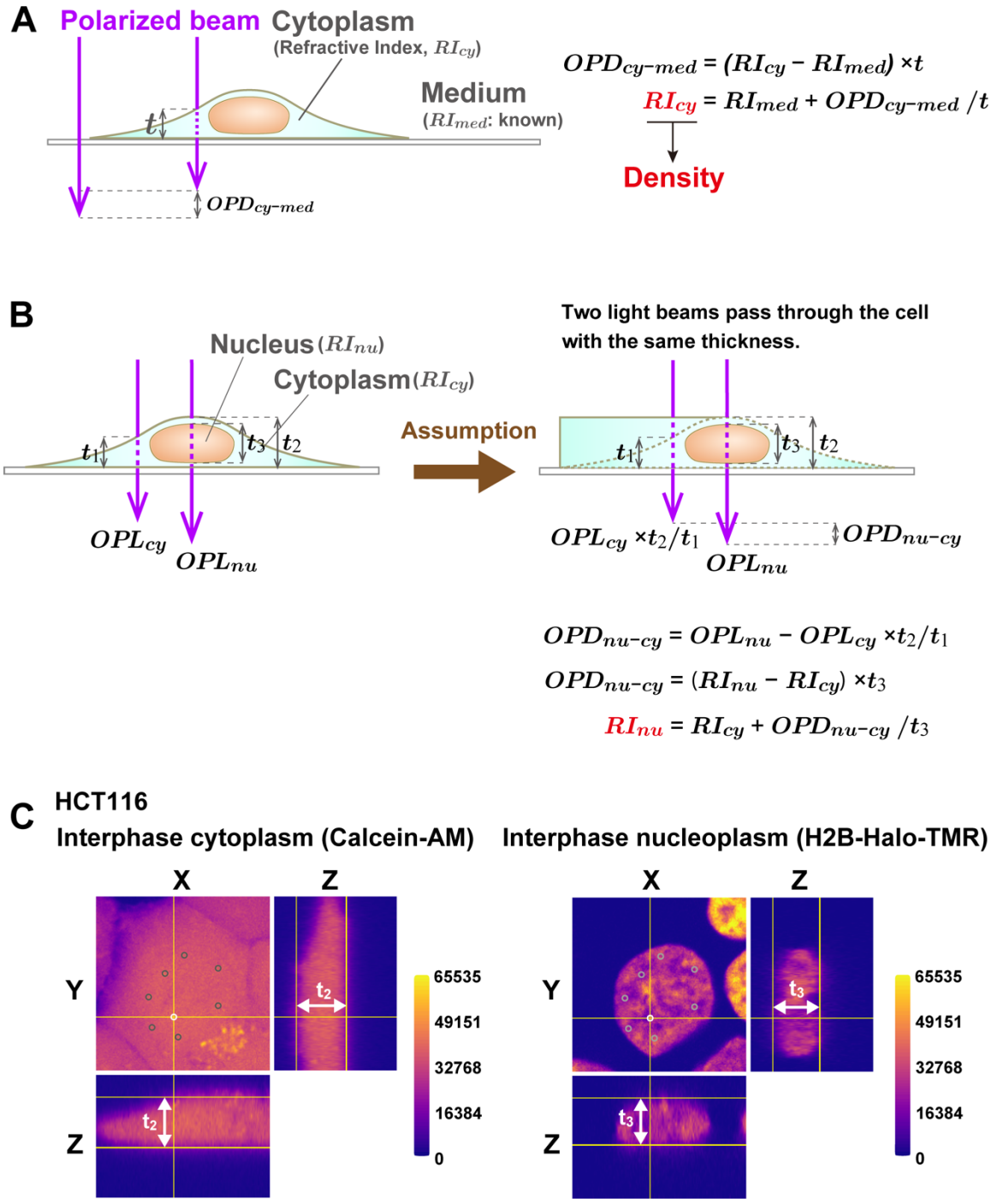

Figure S3.

A simple schematic of the method used to estimate the refractive index (RI) in interphase cells.

(A) The cytoplasm RI_{cy} can be calculated based on the OPD measured by OI-DIC, the RI of medium (RI_{med}) measured by refractometer, and thickness (t) values. For details, see SI Materials and Methods. **(B)** A calculation scheme for the RI of the nucleus (RI_{nu}). We obtained

RI_{cy} based on the measured values for OPD_{cy-med}, thickness t_1, and RI_{med}. Because the thicknesses of the sample through each of the two polarized beams passed should be the same, we multiplied OPL_{cy} by t_2/t_1 to obtain OPD_{nuc-cy} (t_2, thickest point of the cell including nucleus and cytoplasm; t_1, thickness of cytoplasm region beside nucleus). RI_{nu} was calculated based on RI_{cy} and nuclear thickness t_3. **(C)** Thickness measurement of HCT116 cytoplasm (left) and nucleus (right) to estimate the molecular density of the nucleus. Several points in the nucleus were selected. The threshold for cytoplasm thickness was set at 33% or more for the difference between the maximum and minimum intensity of the z-axis profile of the selected points. For the nucleus, a threshold was also set at 33%. Here, points of thickness indicated by a white circle for the cytoplasm (t_2) or nucleus (t_3) are shown in an orthogonal view. “mpl-plasma” in Fiji was used for LUT (Lookup table). Also see (B).

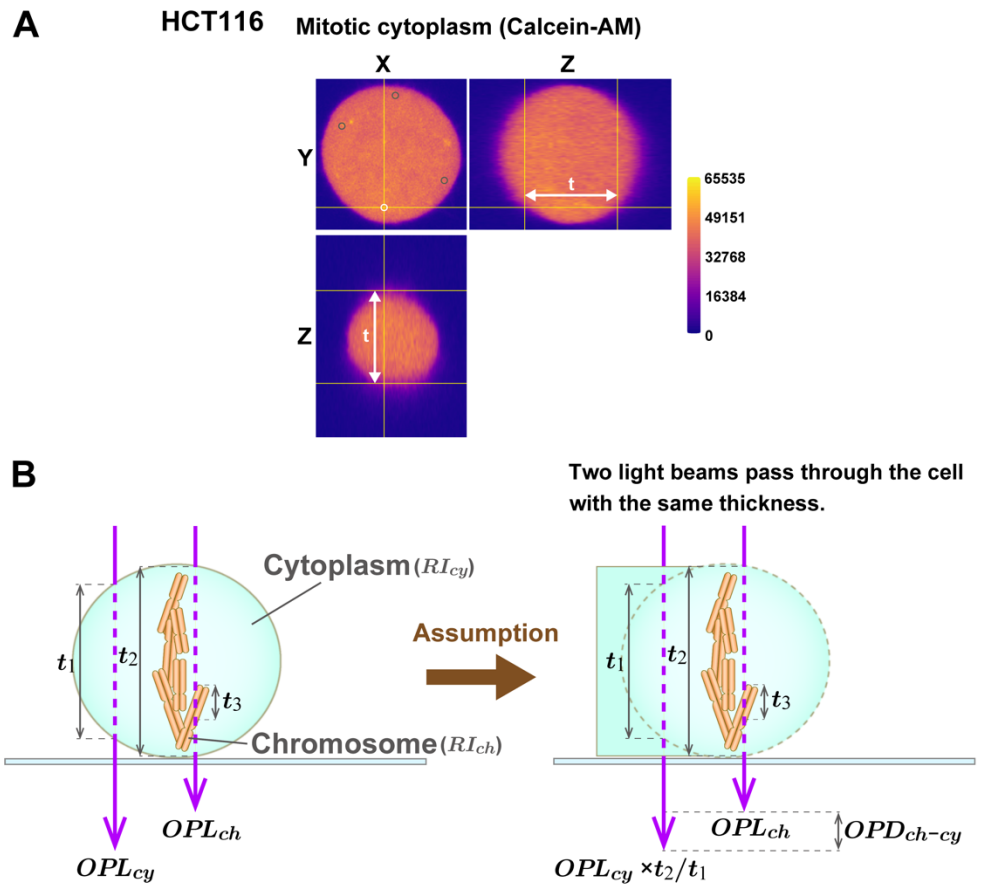

Figure S4.

Simplified schematic of the method to estimate the RI in mitotic cells.

(A) Thickness measurement of HCT116 cytoplasm. Several points that did not overlap with chromosomes were selected. The threshold for thickness was set at 40% or more of the difference between the maximum and minimum intensities of the z-axis profile of the selected points (small white and dark circles). Here, the thickness (t) of the point indicated by a white circle is shown in an orthogonal view. “mpl-plasma” in Fiji was used for LUT. Also see Fig. 2B. **(B)** A calculation scheme for the RI of chromosome (RI_{ch}). We obtained RI_{cy} based on the measured values for OPD_{cy-med}, thickness t_1, and RI_{med}. Because the thicknesses of the sample that the two polarized beams passed through should be the same, we multiplied OPL_{cy} by t_2/t_1, to obtain OPD_{ch-cy} (t_2, thickest point of the cell including chromosome and cytoplasm; t_1, thickness of cytoplasm region with chromosome-free). RI_{ch} was calculated based on RI_{cy} and chromosome thickness t_3. **(C)** Thickness measurements of Indian Muntjac DM cytoplasm (left) and chromosomes (right) to estimate the molecular density of chromosomes. Several points were selected where chromosomes were present without overlapping. The thickness threshold for cytoplasm was set at 40% or more of the difference between the maximum and minimum intensities of the z-axis profile of the selected points. For chromosomes, a threshold was set at 33%. Here, cytoplasm thickness (t_2) and chromosome thickness (t_3) of the point indicated by a white circle are shown in an orthogonal view. “mpl-plasma” in Image J was used for LUT. Also see (B).

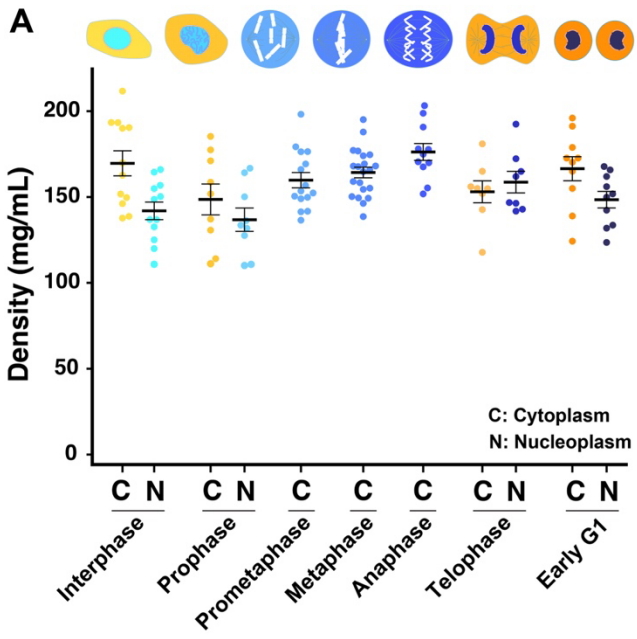

B

HCT116 cells	Density (mg/mL)
Interphase cytoplasm	170 ± 25.3
Interphase nucleoplasm	142 ± 17.8
Prophase cytoplasm	148 ± 27.0
Prophase nucleoplasm	137 ± 20.4
Prometaphase cytoplasm	160 ± 17.2
Metaphase cytoplasm	164 ± 14.1
Anaphase cytoplasm	176 ± 16.2
Telophase cytoplasm	153 ± 18.1
Telophase nucleoplasm	158 ± 17.8
Early G1 cytoplasm	167 ± 22.1
Early G1 nucleoplasm	148 ± 15.2
Nucleolus: ~211 mg/mL	(data from Fig. S10)

Figure S5.

Total molecular density in live mitotic HCT116 cells.

(A) Total molecular densities of chromosome milieu gradually increased with the progression from prophase to anaphase in live HCT116 cells. Cytoplasm density dropped when the cell morphology changed (Prophase, Telophase). Cytoplasm density was lower than nucleoplasm density at Telophase, and then increased in Early G1, presumably by compartmentalization through nuclear envelope reformation. Each dot represents the average of the estimated total density at several points within a single cell (e.g., Fig. S2). N, Nucleoplasm; C, Cytoplasm. Mean ± SE are shown by error bars. Cell numbers are $N = 12$ (Interphase), $N = 9$ (Prophase), $N = 15$ (Prometaphase), $N = 21$ (Metaphase), $N = 11$ (Anaphase), $N = 8$ (Telophase), $N = 10$ (Early G1). **(B)** Mean ± SD values of total molecular densities at each phase of HCT116 cells. Data of Interphase nucleoplasm, Prophase nucleoplasm, Prometaphase cytoplasm, Metaphase cytoplasm, Anaphase cytoplasm, Telophase nucleoplasm, and Early G1 nucleoplasm were reproduced from Fig. 2D and E.

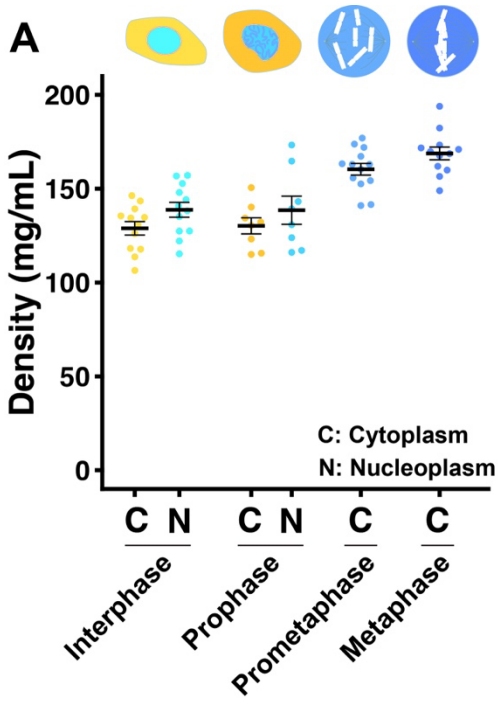

B

DM cells	Density (mg/mL)
Interphase cytoplasm	129 ± 12.5
Interphase nucleoplasm	139 ± 13.7
Prophase cytoplasm	130 ± 12.1
Prophase nucleoplasm	139 ± 21.2
Prometaphase cytoplasm	160 ± 11.2
Metaphase cytoplasm	169 ± 11.7

Figure S6.

Total molecular density in live mitotic Indian Muntjac DM cells.

(A) Total molecular densities of chromosome milieu gradually increased with the progression from prophase to metaphase in live DM cells. Each dot represents the average of the estimated total density at several points within a single cell (e.g., Fig. S2). N, Nucleoplasm; C, Cytoplasm. Mean ± SE are shown by error bars. Cell numbers are *N* = 12 (Interphase), *N* = 8 (Prophase), *N* = 13 (Prometaphase), and *N* = 12 (Metaphase). **(B)** Mean ± SD values of total molecular densities at each cell cycle phase of DM cells. Data of Interphase nucleoplasm, Prophase nucleoplasm, Prometaphase cytoplasm, and Metaphase cytoplasm were reproduced from Fig. 3B and C.

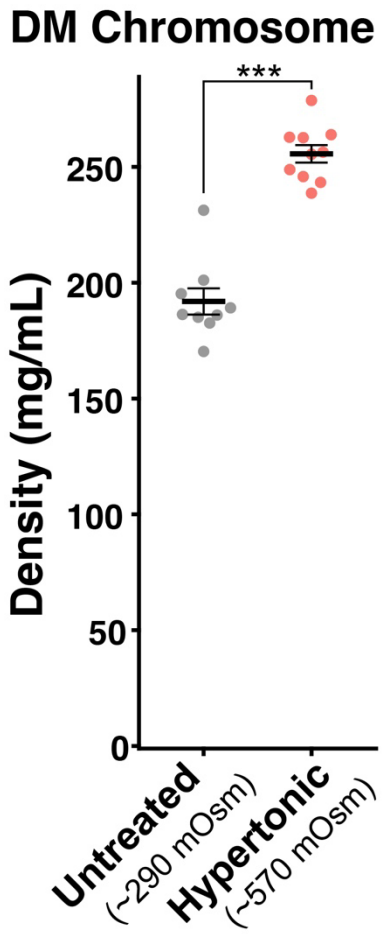

DM cells	Density (mg/mL)
Untreated chromosome	192 ± 17.0
Hypertonic chromosome	256 ± 11.9

Figure S7.
Density imaging of chromosomes in live mitotic Indian Muntjac DM cells.
Hypertonic treatment increases the total densities of chromosomes in live mitotic DM cells. Each dot represents the average of the estimated total density at several points of chromosomes within a single cell. Mean ± SE are shown by error bars. Cell numbers are $N = 9$ (Untreated) and $N = 10$ (Hypertonic). ***, $P < 0.0001$ by the two-sided unpaired t-test ($P = 1.9 \times 10^{-7}$). The table shows mean ± SD values.

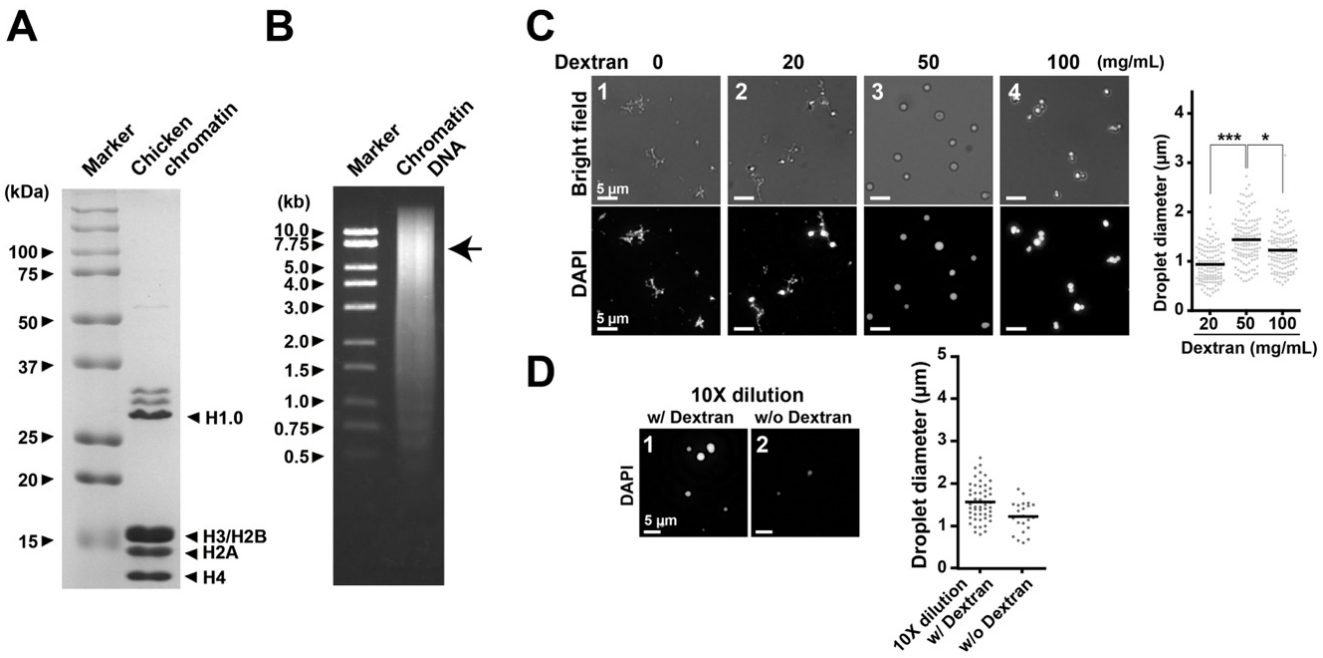

Figure S8.

Chicken native chromatin preparation and droplet formation with Dextran.

(A) SDS-PAGE of purified chicken native chromatin. Coomassie Brilliant Blue (R-250) staining shows that nucleosome core histones H2A/H2B, H3, and H4, as well as linker histone H1.0, are present in the sample. **(B)** Agarose gel of purified chromatin DNA. Average DNA length is ~6 kb (shown by arrow). **(C)** Formation of chromatin condensates/droplets with physiological salt and Dextran (~200 kDa). Fibrous chromatin condensates were induced by 100 mM K^+ and 0.8 mM Mg^{2+} (Panel 1, 0 mg/mL Dextran). An increase in Dextran converted the fibrous condensates into droplets (Panels 2 and 3). A further increase in Dextran put the droplets together without fusions, suggesting the solid-like properties of the droplets (Panel 4). Diameters of formed droplets are shown on the right plots. ***, $P < 0.0001$ by Wilcoxon rank sum test for 20 mg/mL vs. 50 mg/mL PEG ($P = 7.2 \times 10^{-17}$). *, $P < 0.05$ for 50 mg/mL vs. 100 mg/mL PEG ($P = 2.0 \times 10^{-4}$). **(D)** The droplet dilution assay. After the droplets were formed with 50 mg/mL of Dextran, the reaction mixtures were diluted 10-fold in a buffer with (Panel 1) or without (Panel 2) 50 mg/mL of Dextran. Panel 2 depicts fewer and smaller droplets than Panel 1, suggesting that the droplets were dissolved in the diluted buffer without Dextran. A quantitative analysis of the droplet dilution assay (right). The amount and diameters of droplets from a randomly picked areas (6.0×10^4 μm^2) are plotted.

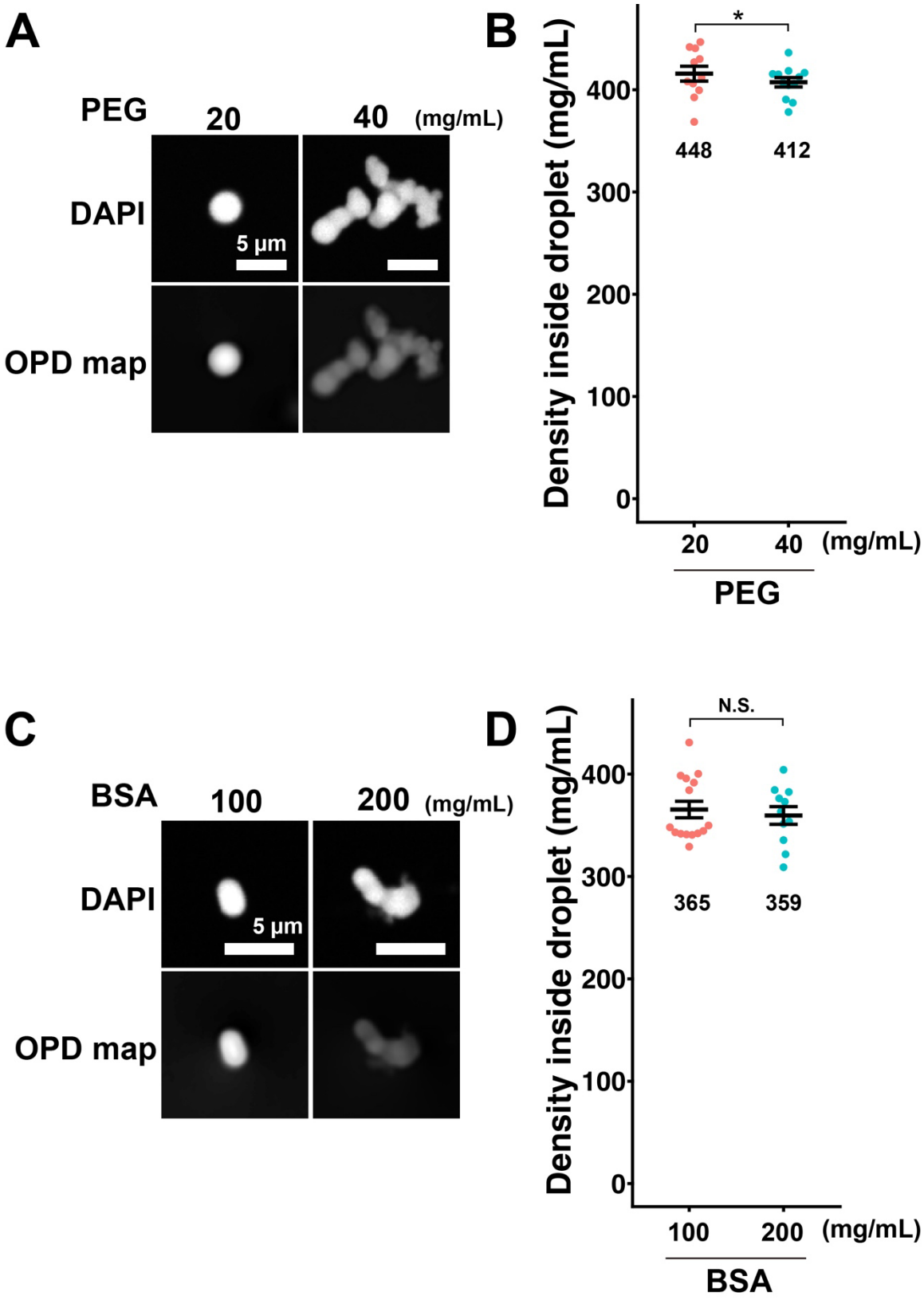
A
PEG
20
40
(mg/mL)
DAPI
5 μm
OPD map
B
*
Density inside droplet (mg/mL)
448
412
0
100
200
300
400
20
40
(mg/mL)
PEG
C
BSA
100
200
(mg/mL)
DAPI
5 μm
OPD map
D
N.S.
Density inside droplet (mg/mL)
365
359
0
100
200
300
400
100
200
(mg/mL)
BSA

Figure S9.
Density imaging of chromatin droplets.

DAPI-stained chicken native chromatin droplets were imaged using an OI-DIC microscope. Droplets formed into larger droplets without fusing when incubated up to 1 h in **(A)** 40 mg/mL PEG or **(C)** 200 mg/mL BSA. Note that the OPD maps show the difference in OPL between the solution and the droplets; solution density affects the OPD map intensity. **(B)** An increase in the PEG concentration did not increase the density of chromatin droplets. Droplet numbers were N = 18 (20 mg/mL PEG) and N = 13 (40 mg/mL PEG). *, $P < 0.05$ ($P = 7.9 \times 10^{-3}$). **(D)** An increase in the BSA concentration did not significantly affect the density of chromatin droplets. Droplet numbers were N = 15 (100 mg/mL BSA) and N = 11 (200 mg/mL BSA). N.S., not significant (P = 0.63). **(B, D)** Each dot represents the average of the estimated total density at several points within a droplet. Mean ± SE are shown by error bars. The average densities of droplets (mg/mL) are shown below the plots. P was determined using the two-sided unpaired t-test.

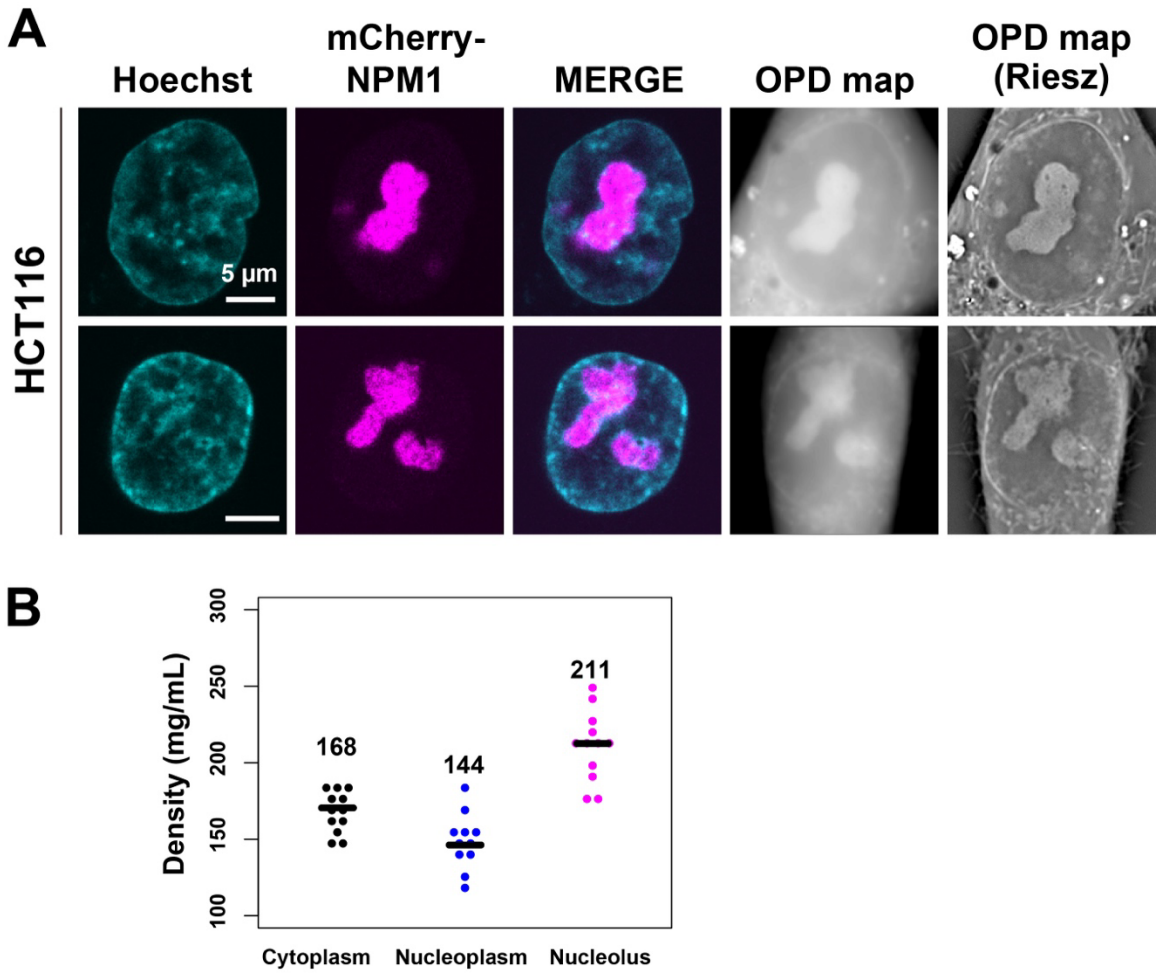

Figure S10.

Density imaging of the nucleolus.

(A) Live HCT116 cell confocal images of DNA (Hoeschst) and nucleoli (mCherry-NPM1), and OI-DIC generated OPD and OPD-Riesz maps. Riesz images are edge-enhanced OPD maps according to the inverse Riesz transform. **(B)** Total molecular densities of interphase cytoplasm, nucleoplasm, and nucleolus in live HCT116 cells. Each dot represents the average of the estimated total density at several points within a single cell. For details, see Materials and Methods. Black bars show the mean. Cell numbers are *N* = 12 (Interphase cytoplasm), *N* = 11 (Interphase nucleoplasm), and *N* = 12 (Nucleolus).

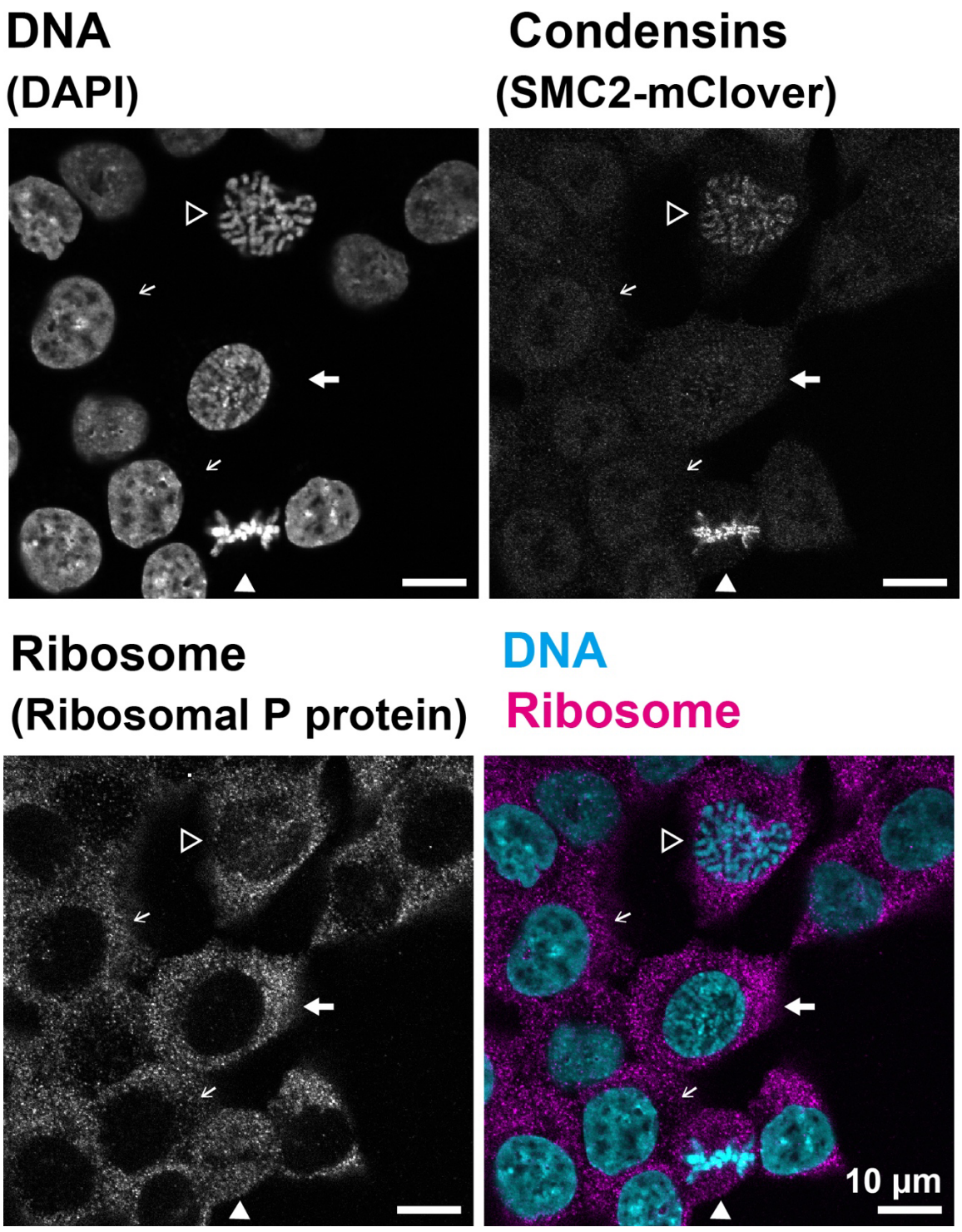

Figure S11.

Localization of ribosomes revealed by immunostaining.

Confocal images of asynchronous HCT116 cells are shown. Interphase cells are indicated by thin arrows, prophase by a thick arrow, prometaphase by an outlined arrowhead, and metaphase by a filled arrowhead. Condensins are visualized by mClover-tagged endogenous SMC2, the common

subunit of condensins I and II. Note that during interphase and prophase, prior to nuclear envelope break down, ribosomes are sequestered from chromatin by the nuclear membrane. After nuclear envelope break down (prometaphase and metaphase), ribosomes can come into contact with chromosomes.

Table S1.
Refractive index (RI) of HCT116 cells.

HCT116 cells	Refractive index (RI)
Interphase cytoplasm	1.362 ± 0.005044
Interphase nucleoplasm	1.356 ± 0.002929
Prophase cytoplasm	1.358 ± 0.004460
Prophase nucleoplasm	1.356 ± 0.003369
Prometaphase cytoplasm	1.359 ± 0.002841
Metaphase cytoplasm	1.360 ± 0.002323
Anaphase cytoplasm	1.363 ± 0.003487
Telophase cytoplasm	1.358 ± 0.002984
Telophase nucleoplasm	1.359 ± 0.002929
Early G1 cytoplasm	1.361 ± 0.003649
Early G1 nucleoplasm	1.358 ± 0.002509
Mitotic cytoplasm (with hypertonic treatment)	1.373 ± 0.003120
Mitotic cytoplasm (with hypotonic treatment)	1.348 ± 0.003112

Table S2.
Refractive index (RI) of DM cells.

DM cells	Refractive index (RI)
Interphase cytoplasm	1.354 ± 0.002060
Interphase nucleoplasm	1.356 ± 0.002264
Prophase cytoplasm	1.355 ± 0.002000
Prophase nucleoplasm	1.356 ± 0.003500
Prometaphase cytoplasm	1.360 ± 0.001850
Metaphase cytoplasm	1.361 ± 0.001938
Metaphase chromosome	1.365 ± 0.002810
Mitotic cytoplasm (with hypertonic treatment)	1.378 ± 0.002636
Mitotic chromosome (with hypertonic treatment)	1.376 ± 0.002238
Mitotic cytoplasm (with hypotonic treatment)	1.345 ± 0.003309

Movie S1 (separate file).

Bright field movie of fusions of chromatin liquid droplets formed in the presence of 20 mg/mL of PEG (10 s/frame). Three fusion events were recorded in total.

SI References

1. E. M. Manders, H. Kimura, P. R. Cook, Direct imaging of DNA in living cells reveals the dynamics of chromosome formation. *J Cell Biol* **144**, 813-821 (1999).
2. R. Nagashima *et al.*, Single nucleosome imaging reveals loose genome chromatin networks via active RNA polymerase II. *J Cell Biol* **218**, 1511-1530 (2019).
3. A. Yesbolatova *et al.*, The auxin-inducible degron 2 technology provides sharp degradation control in yeast, mammalian cells, and mice. *Nat Commun* **11**, 5701 (2020).
4. T. Natsume, T. Kiyomitsu, Y. Saga, M. T. Kanemaki, Rapid Protein Depletion in Human Cells by Auxin-Inducible Degron Tagging with Short Homology Donors. *Cell Rep* **15**, 210-218 (2016).
5. K. Maeshima *et al.*, Nuclear pore formation but not nuclear growth is governed by cyclin-dependent kinases (Cdks) during interphase. *Nat Struct Mol Biol* **17**, 1065-1071 (2010).
6. S. Ide, R. Imai, H. Ochi, K. Maeshima, Transcriptional suppression of ribosomal DNA with phase separation. *Sci Adv* **6** (2020).
7. R. Imai *et al.*, Density imaging of heterochromatin in live cells using orientation-independent-DIC microscopy. *Mol Biol Cell* **28**, 3349-3359 (2017).
8. M. Shribak, K. G. Larkin, D. Biggs, Mapping optical path length and image enhancement using quantitative orientation-independent differential interference contrast microscopy. *J Biomed Opt* **22**, 16006 (2017).
9. M. Shribak, S. Inoue, Orientation-independent differential interference contrast microscopy. *Appl Opt* **45**, 460-469 (2006).
10. M. Shribak, Quantitative orientation-independent differential interference contrast microscope with fast switching shear direction and bias modulation. *J Opt Soc Am A Opt Image Sci Vis* **30**, 769-782 (2013).

11. J. E. Malamy, M. Shribak, An orientation-independent DIC microscope allows high resolution imaging of epithelial cell migration and wound healing in a cnidarian model. *J Microsc* **270**, 290-301 (2018).
12. Y. Itoh *et al.*, 1,6-hexanediol rapidly immobilizes and condenses chromatin in living human cells. *Life Sci Alliance* **4**, e202001005 (2021).
13. K. Ura, Y. Kaneda, Reconstitution of chromatin in vitro. *Methods Mol Biol* **181**, 309-325 (2001).
14. K. Maeshima *et al.*, Nucleosomal arrays self-assemble into supramolecular globular structures lacking 30-nm fibers. *EMBO J* **35**, 1115-1132 (2016).
15. T. Uchiumi, R. R. Traut, R. Kominami, Monoclonal antibodies against acidic phosphoproteins P0, P1, and P2 of eukaryotic ribosomes as functional probes. *J Biol Chem* **265**, 89-95 (1990).
16. D. Marenduzzo, K. Finan, P. R. Cook, The depletion attraction: an underappreciated force driving cellular organization. *J Cell Biol* **175**, 681-686 (2006).